ADVANCED MATERIALS
www.advmat.de

Electrolytes with Solvating Inner Sheath Engineering for Practical Na–S Batteries

*Dong Guo, Jiaao Wang, Tianxing Lai, Graeme Henkelman, and Arumugam Manthiram**

Sodium–sulfur (Na–S) batteries with durable Na-metal stability, shuttle-free cyclability, and long lifespan are promising to large-scale energy storages. However, meeting these stringent requirements poses huge challenges with the existing electrolytes. Herein, a localized saturated electrolyte (LSE) is proposed with 2-methyltetrahydrofuran (MeTHF) as an inner sheath solvent, which represents a new category of electrolyte for Na–S system. Unlike the traditional high concentration electrolytes, the LSE is realized with a low salt-to-solvent ratio and low diluent-to-solvent ratio, which pushes the limit of localized high concentration electrolyte (LHCE). The appropriate molecular structure and solvation ability of MeTHF regulate a saturated inner sheath, which features a reinforced coordination of Na^+ to anions, enlarged Na^+-solvent distance, and weakened anion-diluent interaction. Such electrolyte configuration is found to be the key to build a sustainable interphase and a quasi-solid–solid sulfur redox process, making a dendrite-inhibited and shuttle-free Na–S battery possible. With this electrolyte, pouch cells with decent cycling performance under rather demanding conditions are demonstrated.

1. Introduction

The battery community has made extensive efforts to develop lithium–sulfur (Li–S) batteries in the past decade because of the low cost and high theoretical capacity (1675 mA h g^{-1}) of sulfur.[1–5] Nevertheless, if we consider that sodium is much more earth-abundant (2.3 wt.%) than lithium (0.0017 wt.%) and globally accessible, room-temperature (RT) sodium–sulfur (Na–S) battery is a more sustainable solution to large-scale energy storage. The RT Na–S battery could deliver a theoretical energy density of 1274 Wh kg^{-1}, while the price of Na raw material is <1/25 that of Li.[6] Yet, the RT Na–S system is still in its infancy and is much more challenged than the Li–S analogues by the issues, including poor utilization of electrode materials, severe self-discharge, and short cycle lifespan.[7–9]

Electrolyte engineering is believed to be the core and pragmatic solution. This is because the issues in Na–S batteries essentially arise from the poor compatibility between electrolyte and electrodes. At the cathode side, the sodium polysulfide (NaPS) intermediates are highly soluble in ether-based electrolytes, which causes much more exacerbated shuttling effect than Li–S system.[9–14] The carbonate-based solvents could even participate in irreversible side reactions with NaPS, resulting in a rapid capacity decay. As for the anode, the decomposition of traditional electrolytes on Na metal is uncontrollable (**Figure 1**a), which induces undesired solid-electrolyte interphases (SEIs) and degradation of both the electrolyte and Na metal.[15–19] In this context, designing suitable electrolytes to modulate the interfacial compatibility is an imperative pathway.

Fundamentally, the properties of bulk electrolytes are governed by the local coordination between solvents and anions with cations. It has been established that anions recruited into the solvation sheath of cations have decreased lowest unoccupied molecular orbital (LUMO), which preferentially decomposes on anode before the solvents, thereby forming inorganic-rich SEIs to protect the electrode.[20–23] Derived from high concentration electrolyte (HCE), localized high-concentration electrolyte (LHCE) is an effective practice in this regard.[20,24–28] Due to the reduced number of solvents, the anions can interact with the cations and enter the inner solvation sheath, forming an anion-dominated solvation structure that features contact ion pairs (CIP) and aggregated ion pairs (AIP) rather than solvent-separated ion pairs (SSIP; Figure 1a). Nevertheless, most of the solvents in the inner shell are strong solvating molecules, including the typical ether-based 1,2-dimethoxyethane (DME).[29] This means, extremely high salt-to-solvent ratio (SSR) and diluent-to-solvent ratio (DSR) is still required to realize the desired CIP structure, which inevitably incur low ionic conductivity and high cost.[30] More importantly, in the Na–S system, the solvation configuration in the inner-shell not only dictates anode stability, but also controls the sodium polysulfide (NaPS) conversion. However, how the interaction among solvent, diluent, and Na^+-anion/NaPS impact the performance remain elusive, and the design rules are not well established.

D. Guo, T. Lai, A. Manthiram
Materials Science and Engineering Program and Texas Materials Institute
The University of Texas at Austin
Austin, TX 78712, USA
E-mail: rmanth@mail.utexas.edu
J. Wang, G. Henkelman
Department of Chemistry
The University of Texas at Austin
Austin, TX 78712, USA

The ORCID identification number(s) for the author(s) of this article can be found under https://doi.org/10.1002/adma.202300841

DOI: 10.1002/adma.202300841

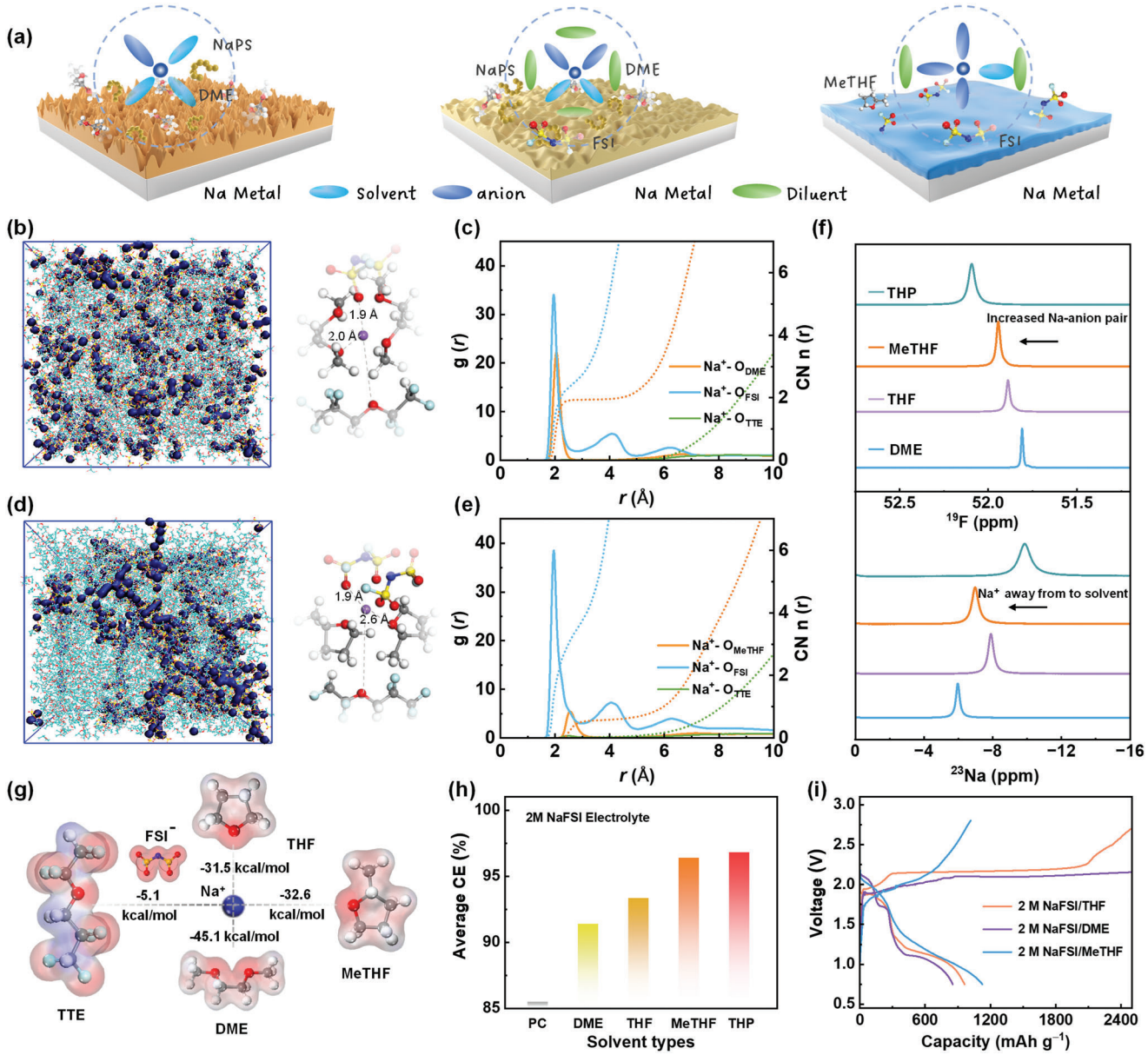

Figure 1. a) Schematic solvation structures of different electrolytes (left: low concentration; middle: LHCE; right: proposed MeTHF based electrolytes) and the corresponding interfacial compatibility of NaPS/electrolytes on Na anode. Snapshots and the corresponding RDFs of b,c) 2 M NaFSI in DME/TTE andd,e) 2 M NaFSI in MeTHF/TTE from MD simulation. f) ^{23}Na and ^{19}F NMR spectra of 2 M NaFSI in various solvents. g) Electrostatic potential maps of the various solvents and their corresponding binding energies with Na^+. h) CEs of Na–Cu cells with 2 M NaFSI in different solvents cycled at 1.0 mA cm^{-2}, 1.0 mAh cm^{-2}. i) Typical voltage curves of Na–S batteries with different solvents.

Herein, by using a cyclic ether (2-methyltetrahydrofuran, MeTHF) as an inner-shell cosolvent, a new type of electrolyte is proposed for Na–S batteries. We find that compared with the typical linear ether DME and cyclic ether tetrahydrofuran (THF), the MeTHF has a lower solvation energy and a slightly larger steric hindrance. This allows the anion species approach closer to the Na^+ cation in the inner sheath, while the solvents remain closer to the diluent in the outer shell. Such spatial coordination enables the electrolyte transform from LHCE to localized saturated electrolyte (LSE) at low SSR and DSR conditions (Figure 1a). In such electrolyte systems, a more rigid and efficient SEI layer is formed on Na-metal anode, regardless of the similar Li growth behavior. Meanwhile, the sulfur conversion on cathode is shifted from conventional dissolution–precipitation chemistry to a quasi-solid-state reaction. Thereby, remarkably improved CEs and sulfur utilization are achieved in pouch cells, albeit no optimization on the test conditions. Our results indicate that the higher the solvating power of inner-shell solvent, the more severe will be the NaPS dissolution and the lower CE with the Na–S cell. By contrast, a moderate solvating power of inner-shell solvent is a better choice in Na–S cells.

2. Results and Discussion

We screened potential solvents via both theoretical and experimental means. Dilute electrolytes were first formulated by dissolving 2.0 M sodium bis(fluorosulfonyl)imide (NaFSI) into four representative ethereal solvents, including DME, tetrahydrofuran (THF), MeTHF, and tetrahydropyran (THP) due to their distinct features. To investigate the intrinsic coordination ability of the solvents, the binding energy ($\Delta G_{binding}$) between single solvent molecule and Na^+ was calculated. The density functional theory (DFT) calculation results reveal the largest $\Delta G_{binding}$ for DME (−45.1 kcal mol^{-1}), followed by MeTHF, THF, and THP (Figure 1g; Figure S1, Supporting Infromation). The larger $\Delta G_{binding}$ indicates DME has much stronger solvating power because of its higher polarity and bidentate nature. In addition, MeTHF has a slightly larger $\Delta G_{binding}$ than THF because the existence of an extra methyl group at the α position offers electron-donating effect on the oxygen atom. Nevertheless, we found that the larger single-molecular coordination ability does not necessarily mean a higher solvation power in real electrolytes for MeTHF, which is well investigated by the nuclear magnetic resonance (NMR) measurements.

As shown in Figure 1f, for the four solvents with 2 M NaFSI, the ^{19}F NMR of FSI^- shows a trend of downfield (positive) shift from DME to THP. The more positive ^{19}F chemical shift arises from decreased electron density in FSI anions, indicating an enhanced $FSI^{-}\cdots Na^+$ ion pairing in the solvent in the order DME < THF < MeTHF < THP. In return, the stronger $Na^+\cdots FSI^-$ ion pairing intensifies electron density around Na^+, thus causing a more negative ^{23}Na NMR chemical shift from DME to THP as shown in Figure 1f. However, there is an exception: MeTHF electrolyte shows a more positive ^{23}Na shift (−6.9 ppm) than the THF sample (−7.9 ppm). It is noteworthy that a lower Na^+ chemical shift results from either a stronger ion solvation or an increased ion pairing. The Na^+ in MeTHF receives more electron contribution from FSI^- anion (^{19}F NMR result), but still shows a more positive ^{23}Na peak than THF. This could be only because of the weaker Na-MeTHF ion solvation, which leads to decreased overall electron density around Na^+. These results are also confirmed by the Radial distribution functions (RDFs) of Na^+ solvation structure as shown in Figure S2 (Supporting Infromation). Therefore, although the extra α-methyl renders MeTHF higher $\Delta G_{binding}$ than THF (Figure 1g), it also causes extra spatial molecular hinderance, which limits the MeTHF coordination with Na^+ center, thus leading to a lower apparent solvation ability. In comparison, THP is the isomer of MeTHF, but without methyl substitution, exhibiting a higher solvation ability (Figure 1f). Overall, MeTHF enables a lower ion solvation ability, yet stronger $Na^+\cdots$anion pairing ability simultaneously, which could not be realized by the other counterparts.

The unique coordination properties enable the 2 M NaFSI/MeTHF electrolyte with a high average CE of 96.5% for Na deposition/stripping in Na–Cu cells, which apparently outperforms DME (92.3%) and THF (93.1%) based electrolytes (Figure 1h). The THP-based electrolyte exhibits a comparable CE with MeTHF, but the larger overpotential and lower ionic conductivity excludes it from further optimization (Figure S3–S7, Supporting Infromation). Meanwhile, we found that MeTHF exhibits a distinctive discharge behavior for sulfur conversion. As shown in Figure 1i, the Na–S cell with the DME and THF electrolytes display a typical "slope followed by a plateau" discharge profile, indicative of the typical dissolution–precipitation redox process. The long sloping plateau indicates large number of NaPS dissolved in electrolytes, which causes severe NaPS shuttling, as reflected by the extremely low CE of the THF electrolyte, and the DME cell even failed to charge back to 2.8 V. In contrast, MeTHF based electrolyte enables a quasi-single-sloping discharge profile and a much higher initial discharge capacity, suggesting the generation of soluble NaPS is suppressed and sulfur utilization is enhanced. The greatly improved CE further proves the advantages of MeTHF for Na–S batteries. Nevertheless, the long-term cycling stability still needs to be improved for practical application (Figure S8, Supporting Infromation).

In order to further optimize the electrolyte performance, a non-solvating 1,1,2,2-tetrafluoroethyl-2,2,3,3-tetrafluoropropyl ether (TTE) was added as diluent. The diluent generally does not participate in the coordination, but it could dramatically influence the solvation structure. We noticed that although 3.3 M NaFSI could be fully dissolved in MeTHF, adding TTE diluent causes the salt out from the electrolyte. By adjusting the TTE content in the solution, 2 M NaFSI in MeTHF/TTE (3:2 v/v) approached the saturated state, which is termed as a localized saturated electrolyte (LSE). On the contrary, the DME-based electrolyte could not be saturated with the same concentration due to the high solvation ability, which only forms a LHCE. Compared with the typical LHCE requiring high SSR (salt/solvent > 1:2) and high DSR (diluent/solvent > 1:1), MeTHF takes a much lower diluent/solvent ratio (1:2.7) and low salt/solvent (1:2.6) ratio to achieve the LSE, which is of significance to reduce the cost of the electrolyte. More importantly, such an LSE reaches the critical saturation point in solution, which inherits the merits of MeTHF and further upgrades the solvation structure by reinforcing ion pairing for a better performance as discussed below.

Raman spectroscopy (Figure S9, Supporting Infromation) demonstrate that when TTE is added into 2 M NaFSI/MeTHF to form the LSE, the S–N–S bending peak of FSI^- redshifts from 738 to 749 cm^{-1}, indicating the contact ion-pair between Na^+ and FSI^- is enhanced. Compared with the peak of the associated solid NaFSI at 752 cm^{-1}, the FSI^- anions in LSE behave more like in a quasi-solid state. This local solvation environment is further quantified by molecular dynamics (MD) simulations. Radial distribution functions (RDFs) in Figure 1e show a sharp g(r) peak of Na-O_{FSI} pairs at 1.9 Å, a weak peak of Na–O_{MeTHF} at 2.6 Å, and a negligible peak of Na–O_{TTE}, confirming the inner shell of LSE is dominated by Na-FSI ion pair and surrounded by TTE outer shell. The time-averaged coordination number (CN) is calculated to be 3.9 O_{FSI} and 0.5 O_{MeTHF} per Na^+, denoted as $Na^+(O_{FSI})_{3.9}$-$(O_{MeTHF})_{0.5}$, which is the characteristic CIP/AIP structure, as captured from the snapshot in Figure 1b. This anion reinforced inner shell of LSE enables a preferred decomposition of anion clustered as evaluated by the LUMO energy levels in Figure S10 (Supporting Infromation). In comparison, the DME-based LHCE forms $Na^+(O_{FSI})_{2.8}$-$(O_{DME})_{1.9}$ with more DME and less anions occupied in the solvation inner shell (Figure 1d,e). Moreover, from the RDF we find that the $Na^+\cdots FSI^-$ distance is almost the same (1.9 Å) in the two electrolytes, but the $Na^+\cdots$MeTHF distance (2.6 Å) is significantly larger than the $Na^+\cdots$DME distance (2.0 Å). This means MeTHF keeps relatively

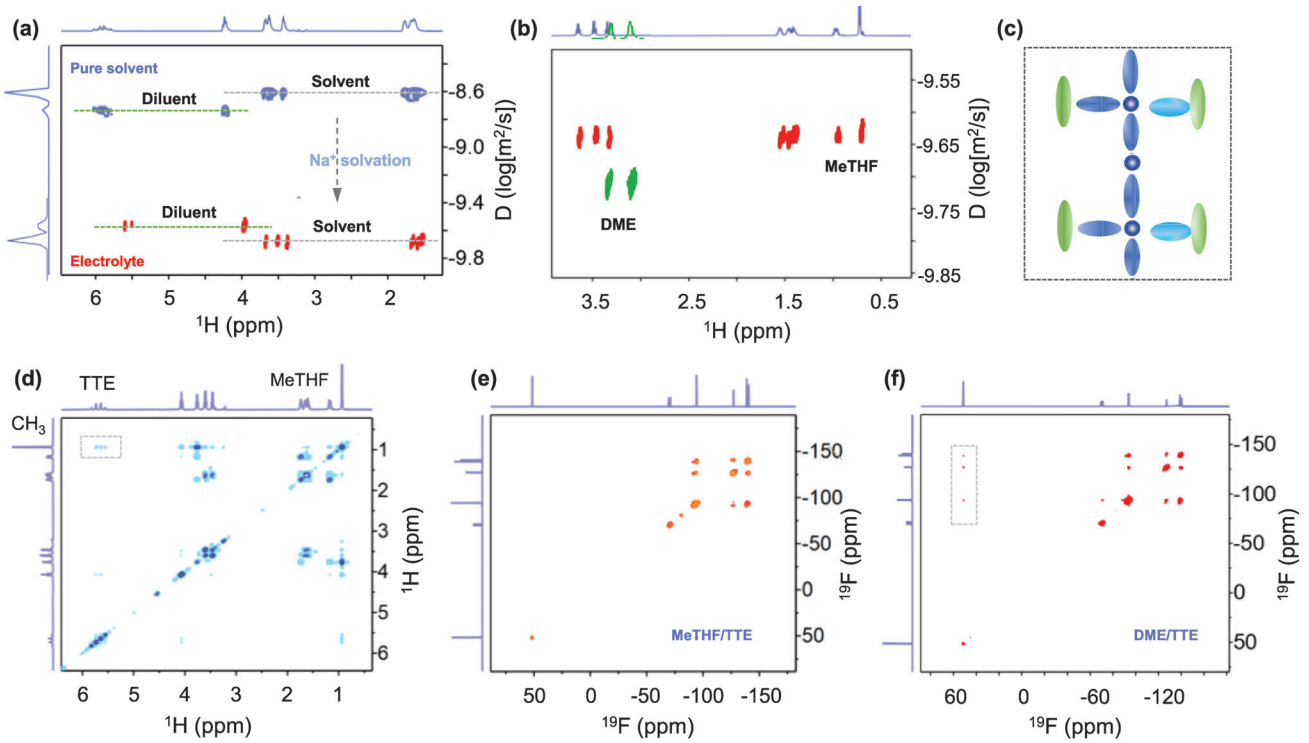

Figure 2. Analysis of the solvation states by 2D NMR. ^{1}H DOSY-NMR spectra of a) MeTHF/TTE mixture and 2 M NaFSI in MeTHF/TTE, and b) 2 M NaFSI in DME/TTE. c) Schematic illustration of the Na^+ solvation configuration in the MeTHF based LSE. d) ^{1}H–^{1}H COSY spectra of 2 M NaFSI in MeTHF/TTE. ^{19}F–^{19}F COSY spectra of 2 M NaFSI in e) MeTHF/TTE and f) in DME/TTE.

far from Na^+ center in the inner shell. This is a favorable spatial coordination because during Na deposition, it may be expected that only the components closely coordinated with Na^+ could be vastly dragged into electrical double layer (EDL) and thereafter be preferentially reduced.[31] The MeTHF with a larger Na^+···MeTHF distance coupled with a lower solvation power would be less likely to be recruited into the EDL than the closely bonded DME, thus a less decomposition of MeTHF could be expected. On the contrary, FSI^- could be more likely to be reduced due to the relatively enhanced Na^+··· FSI^- interaction in the LSE, which is further elucidated by the MD simulation at the Na/electrolyte interface (Figure S11, Supporting Infromation)

2D NMR spectroscopy further elucidate the solvation environment derived from MD simulation. Diffusion-ordered spectroscopy (DOSY) could interpret the NMR signals of different solvation species according to their diffusion coefficient. As plotted in **Figure 2**a, 2D DOSY shows that the MeTHF solvent diffuses slightly faster (2.6×10^{-10} m^2 s^{-10}) than the TTE diluent in neat MeTHF/TTE mixture (blue signals). This is mixture (blue signals). This is understandable as the larger molecular size of TTE affords lower self-diffusion. However, when 2 M NaFSI is added into the solution, the diffusion coefficient of MeTHF decreases significantly (2.4×10^{-10} m^2 s^{-10}) and is even lower than that of TTE (red signals), indicating MeTHF is involved in the Na^+ solvation complex compared with the relatively free TTE outer sheath. Moreover, MeTHF in the 2 M LSE has a faster self-diffusion than DME in the LHCE, which confirms a weaker/looser binding behavior of MeTHF-Na^+ in the inner sheath (Figure 2c), and reconciles with the MD simulation. Such an inner sheath would benefit a lower possibility of solvent reduction on Na–metal surface. Furthermore, 2D ^{1}H-^{1}H correlation spectroscopy (COSY) in Figure 2d detected a cross peak at 0.85 ppm (inside dash box), which arises from the coupling of methyl proton in MeTHF with the proton in TTE. This coupling signal reveals an additional solvent-diluent interaction. It appears that this intermolecular interaction is directional and stable because except the methyl proton coupling, the coupling of TTE with other cyclic protons is not observed. Meanwhile, 2D ^{19}F–^{19}F COSY (Figure 2f) shows a cross peak (at 52 ppm, inside dash box) related to the FSI^--TTE coupling in DME-based electrolyte, which is, however, absent in the MeTHF-based sample (Figure 2e). The obvious diluent-FSI^- interaction suggests the anions is less closely fixed in the inner sheath and Na^+- FSI^--DME complex is less stable.[32] Instead, the 2D NMR analysis reveals that the MeTHF stay far from Na^+, but closer to TTE, ensuring a reinforced and stabilized Na^+- FSI^- inner sheath.

The stable solvation structure alters the SEI composition. X-ray photoelectron spectroscopy (XPS) depth profiling and time-of-flight secondary ion mass spectrometry (TOF-SIMS) experiments were conducted for the cycled Na-Cu cells. The cells were disassembled after 50 cycles in the discharge state, and the surface of deposited Na was analyzed. The XPS contour mappings display the intensity evolution of different compositions in **Figure 3**a–c. Within the whole sputtering time range, the C–C peak (285 eV) from DME-based LHCE, representing the solvent decomposition, are significantly stronger than that from MeTHF-based LSE, indicating severe DME reduction. In contrast, 2 M

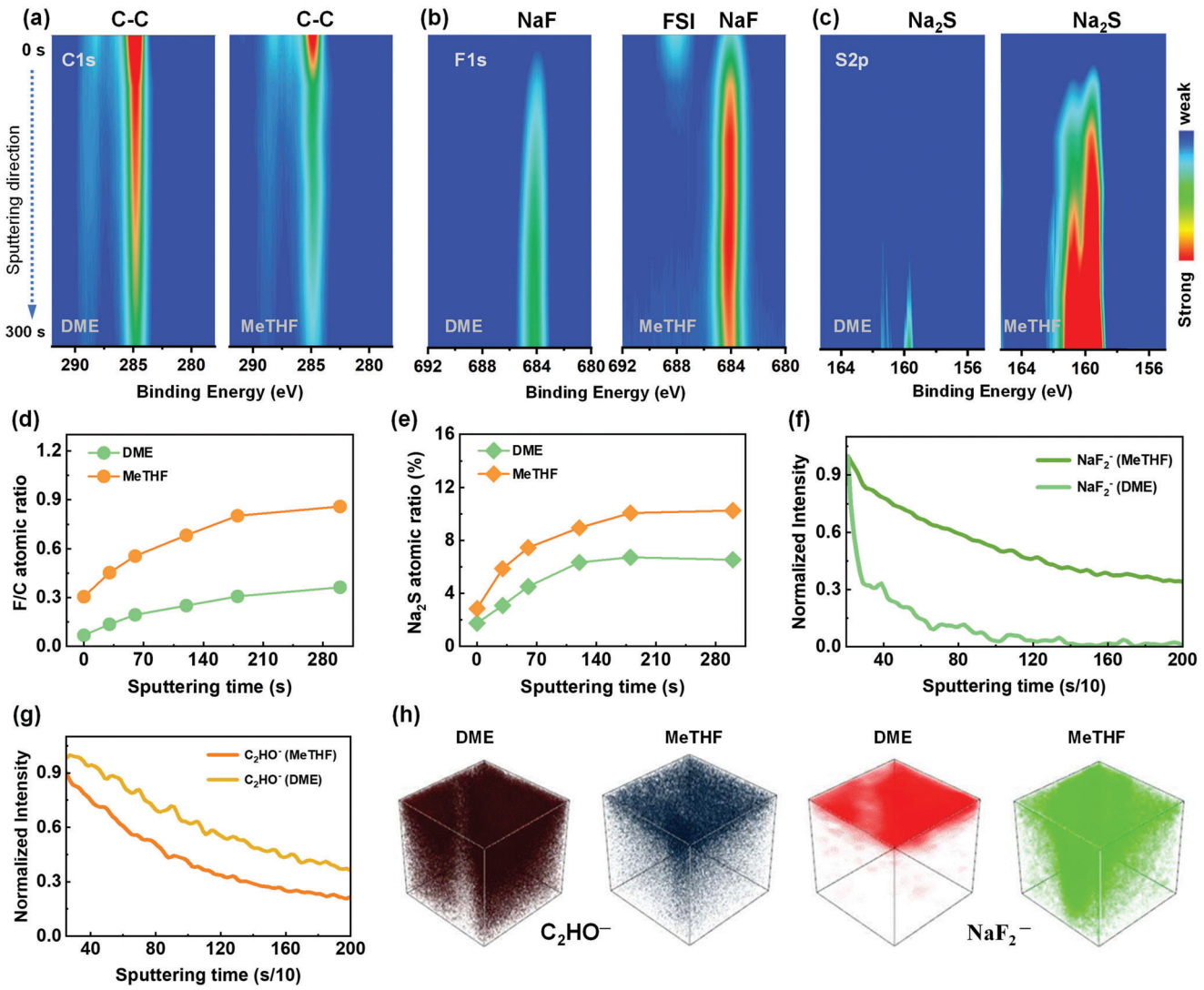

Figure 3. Contour plots of the XPS: a) C1s, b) F1s, and c) S2p spectra of the cycled Na-metal anodes in the two different electrolytes. d) Atomic intensity ratio of F/C peak, and e) areal intensity ratio of the S 2p peak at ≈159.8 eV over the entire S 2p region. f,g) Depth profiles of TOF-SIMS from the cycled Na anodes. h) 3D rendering of TOF-SIMS secondary-ion fragments sputtered from the cycled Na anodes. C_2HO^- refers to the species of solvent decomposition; NaF_2^- represents the product of FSI^- anionic decomposition.

LSE leads to a more complete reduction of FSI^-, as evidenced by the greatly intensified NaF (684 eV) and Na_2S (160 eV) signals in Figure 3b,c. After 2 min of sputtering, the Na-metal anode cycled with 2 M LSE shows two times higher F/C atomic ratio and stronger Na_2S/S(2p) ratio (Figure 3d,e), validating that LSE enabled an inorganic dominated electron–blocking film. The concentration evolution of NaF along sputtering depth exhibits an opposite trend compared with the organic components, suggesting that the decomposition of FSI occurred during the early stage, but was suppressed after the completion of the film-forming process. TOF-SIMS further visualizes a high concentration of organic C_2HO^- fragments occupying the main 3D-rendering space on the Na surface cycled with DME electrolyte. As for LSE, the C_2HO^- signals sharply decreased, and NaF_2^- fragment appears with a much higher spatial occupation after 3D reconstruction. These results clearly point out that in the inner sheath of LSE, a closer Na^+-FSI^- and looser Na^+-MeTHF reconstructed the SEI with inorganic and rigid (further investigated below) protective film, which is the main contributor to resist the continuous corrosion on Na-metal anode.

As shown in **Figure 4**a, the Na-Cu cell with MeTHF-based LSE showed an ultrahigh and stable CE of ≈99.6% regardless of the capacity increasing from 0.5, 1, 2, 3, to 4 mAh cm^{-2}. Noteworthily, negligible polarization increasement was observed during the 600 h of cycling (Figure 4b), which reconciles with the relatively stable interface resistance in Figure 4c and Figures S12–S14 (Supporting Information). By contrast, the CE induced by DME electrolyte is just ≈96.5% at 1 mAh cm^{-2} and jumps to 92% at 4 mAh cm^{-2}. Modified test protocol proposed by Zhang et a.[33] is further employed to more accurately evaluate the average CE. Under 1.0 and 1.0 mAh cm^{-2}, the average CE is calculated to be 99.4% (Figure 4d), which outperform the

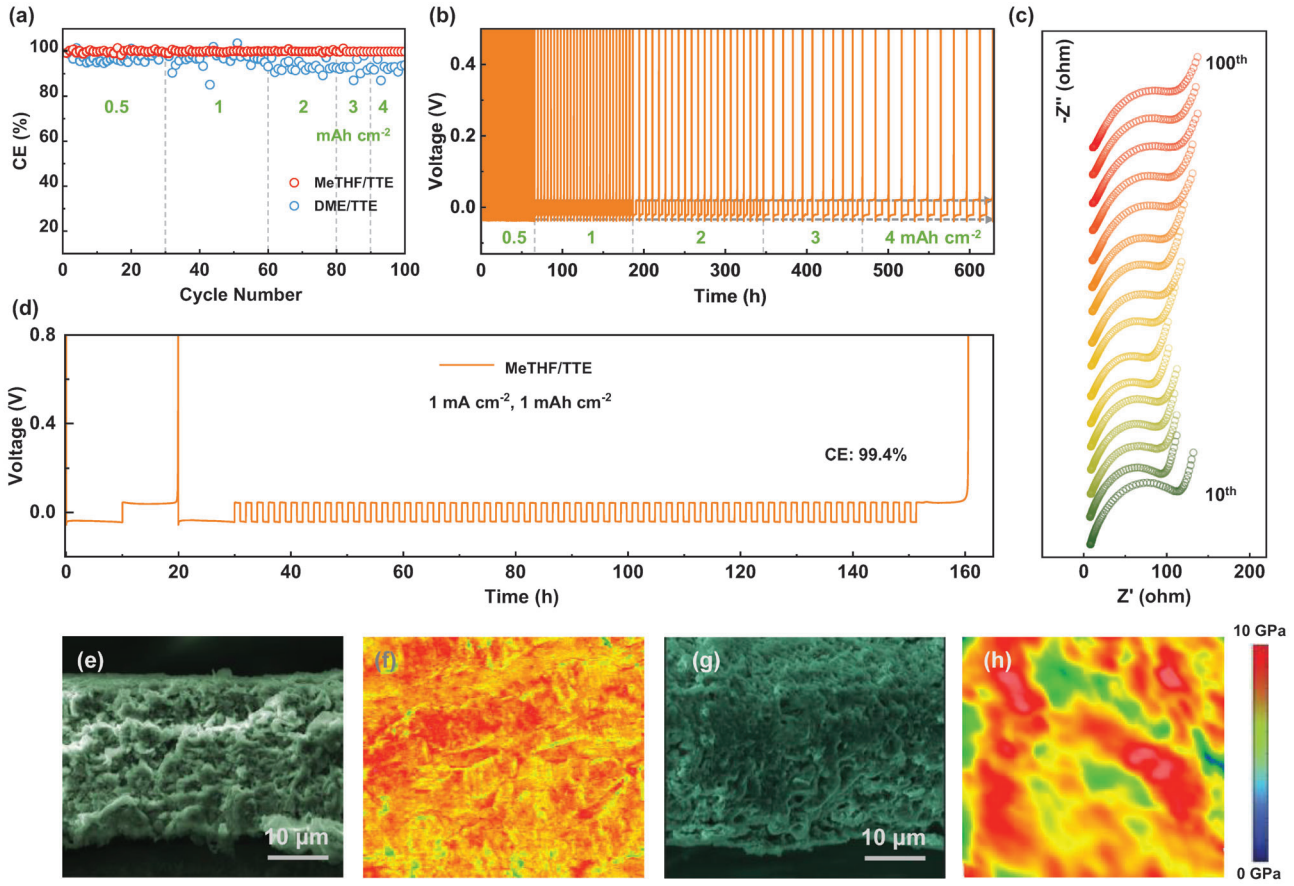

Figure 4. Electrochemical performances of Na–Cu cells under practically relevant conditions. a) CEs and b) voltage curves of Na–Cu cells consecutively cycled at 0.5, 1, 2, 3, and 4 mAh cm^{-2}. c) EIS of the Na–Cu cell cycled with MeTHF based electrolyte. d) Average CE measurements at 1.0 mA cm^{-2}, 1.0 mAh cm^{-2} based on the modified test protocol proposed by Zhang and co-workers.[33] SEM images and modules mappings (2×2 μm) of Na deposits induced by e,f) MeTHF/TTE electrolyte and g,h) DME/TTE electrolyte.

DME based LHCE (Figure S15, Supporting Information) and are among the top record under rather practical conditions.[10,34–37] We note that the Na deposition did not show a significant difference in morphology as shown in Figure 4e,g. However, Young's modulus of the deposits, measured by atomic force microscopy (AFM), is 6.7 GPa in LSE and is two times higher than that of DME-based LHCE (3.1 GPa) (Figure 4f,h). The Young's modulus mapping shows the discrete organic-rich and inorganic-rich regions on the Na anode cycled with DME electrolyte. Although the inorganic species promise to reinforce the SEI, their non-uniform spatial distribution may aggravate the inhomogeneity of ion flux, resulting in severe interfacial instability. As for the LSE electrolyte, the induced inorganic-rich SEI has superior mechanical stiffness and high homogeneity, which is considered the key to offer a durable cycling of Na anode.

The sulfur redox conversion is also mediated on the cathode side. For the two fresh sulfur cathodes, in situ XRD in **Figure 5**a,b and Figure S16 (Supporting Information) show the typical peaks of crystalline S_8 at ≈26.8°and 27.9° (JCPDS no. 008–0247). As the cell with LSE electrolyte is discharged to 1.4 V and below, the peaks of S_8 disappeared, and the strong Na_2S peak at 39° (JCPDS no. 047–1698) appears at the end of the discharge (0.75 V). In the following charge step, the Na_2S peak gradually vanishes coupled with the recovery of S_8 signals, indicating the redox conversion of sulfur is highly reversible in LSE. More importantly, the typical NaPS peaks, such as Na_2S_5 at 31.2°, are not detected during the reaction process, which suggests the conversion between S_8 and Na_2S without the formation of NaPS. This observation also agrees with the corresponding single-sloping discharge curve, which generally represents a quasi solid−solid reaction.[38] By contrast, the Na_2S peak is not detected in the cathode cycled with the DME electrolyte, and S_8 signals could not be recovered after charging back to 2.8 V. This is because the 2 M LHCE could still dissolve number of NaPS, and consequently severe shuttle effect and side reaction is inevitable.

^{23}Na NMR further interprets the states of NaPS in the electrolyte as shown in Figure 5c. ^{23}Na resonance of Na_2S_8 is at 2.8 ppm in LHCE, and greatly shifted downfield to 5.7 ppm in LSE. Since the solvent is a much stronger electron donation ligand than S_8^{2-}, this downfield shift means more polysulfides aggregate around Na^+ to form the quasi-solid-state in LSE. Note that the 1.0 M [S] Na_2S_8 is even not well dissolved in LSE (Figure 5c), and the saturated upper solution is collected for NMR measurement. The MD simulation more precisely reveal

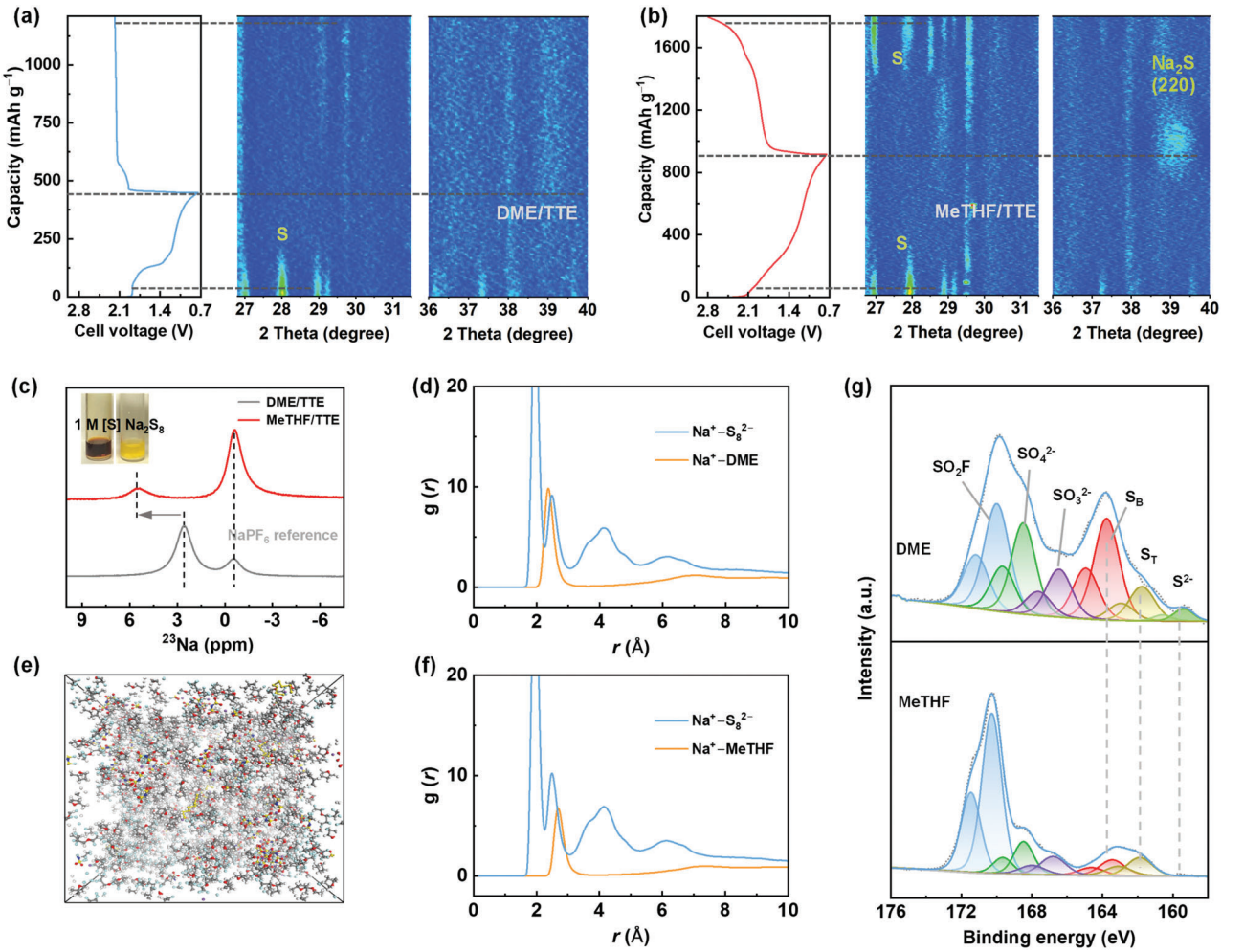

Figure 5. a) In situ XRD contour plot of the Na–S cells in a) DME-based and b) MeTHF-based electrolyte, with the corresponding voltage profiles on the left. c) ^{23}Na NMR spectra of NaPS in the electrolytes, with the inset corresponding to solubility test. d) RDF profile for the Na_2S_8 in DME/TTE and e,f) snapshots and the corresponding RDF of Na_2S_8 in MeTHF/TTE. g) S 2p spectra of Na-metal anode from cycled Na–S cells with the two different electrolytes.

the origin of divergent electrochemical behavior by decoding the solvation environment of NaPS. As shown in the RDF of the 2 M LHCE solution containing 1.0 M [S] Na_2S_8 (Figure 5d), DME and S_8^{2-} emerges, respectively, at 1.9 and 2.3 Å from the center of Na^+ through S_8^{2-}–Na^+–solvent configuration. As for the LSE, MeTHF departs from Na^+ center with 2.7 Å (Figure 5f), and CN of S_8^{2-} around Na^+ increased to 3.9 while CN of MeTHF decreased to 0.7 (Figure S17, Supporting Information). This clearly suggests that Na_2S_8 is more likely to exist as a quasi-solid cluster rather than as an SSIP structure in MeTHF. Therefore, we conclude that for the designed 2 M MeTHF LSE, the electrolyte reaches the saturated state and thus NaPS solubility is limited, which changed the traditional dissolution–precipitation process into a quasi-solid-solid conversion. The XPS of cycled Na–S cell confirms this behavior, as the polysulfide signals (≈164 eV) on Na-metal anode are dramatically weakened in the LSE electrolyte (Figure 5g), indicating the largely inhibited NaPS shuttling.

Consequently, the designed electrolyte enabled impressive capacity performance. As shown in **Figure 6**a,b, the Na–S cell cycled with LSE could maintain a high discharge capacity of 530 mAh g^{-1} after 200 cycles at 0.1 C rate with an average CE of around 100%, which prominently surpass the performance in the DME-based electrolyte (Figure 6b; Figure S18, Supporting Information). Furthermore, a decent rate capacity of 740, 608, 533, and 402 mAh g^{-1} is achieved at 0.2, 0.3, 0.5, and 1 C rates (Figure 6d). When the current density is recovered to 0.1 C rate, the capacity retention is 93.6% of the initial capacity (Figure 6c), reconfirming the durable stability of the electrolyte-engineered battery system. Pouch cells provide more stringent conditions to verify the effectiveness of the designed electrolyte in a large scale. High-loading S cathode (3.2 mg cm^{-2}), ultrathin Na metal anode (≈70 µm), and lean electrolyte (7 µL mg^{-1}) were employed to build a full pouch cell. The initial discharge capacity is ≈670 mAh g^{-1} at 0.1 C rate, and a high-capacity retention of 75% could be retained after 50 cycles (Figure 6e). To the best of our knowledge, the results obtained herein are rather competitive, although the working conditions, such as temperature and packing pressure, were not rationally optimized. Therefore, we believe the developed 2 M MeTHF/TTE based electrolyte would be a promising solution for Na–S batteries. Cathode redox promoters, such as electrochemical catalysis

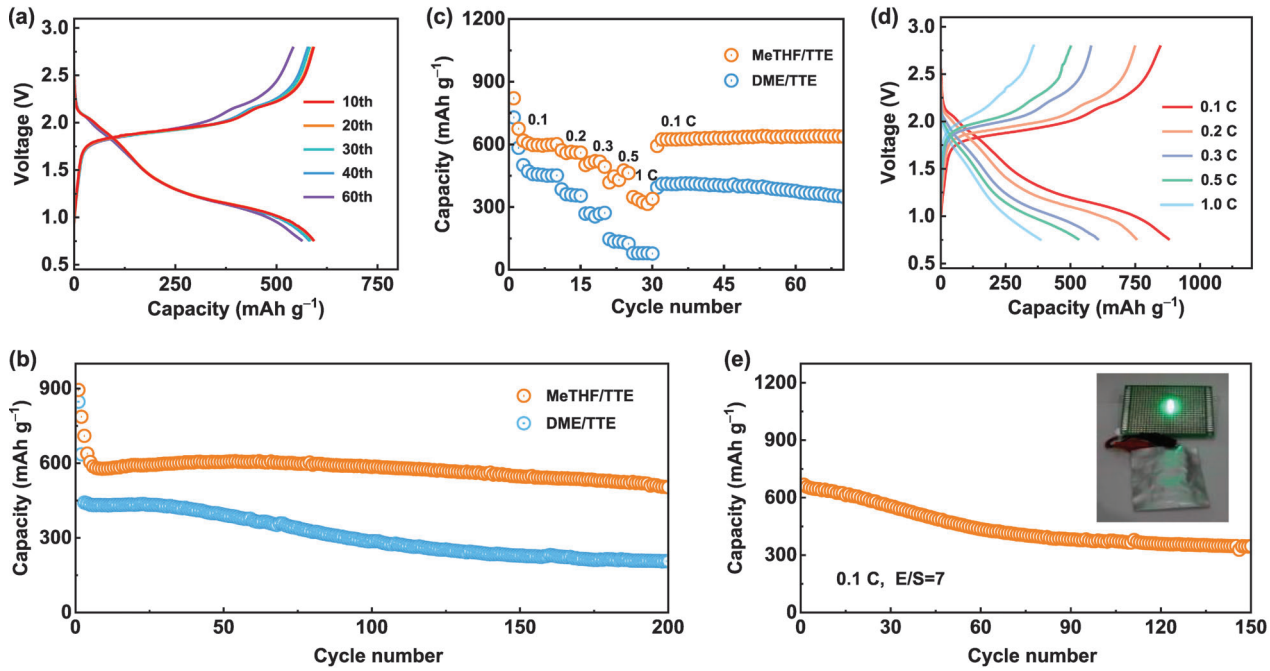

Figure 6. a,b) Discharge–charge profiles of Na–S cell with LSE cycling at 0.1 C rate. b) Cycling performances of the cells with different electrolytes. c) Rate performances. d) Voltage profiles of the cell with the MeTHF/TTE electrolyte. e) Cycling performance of the Na–S pouch cell at 0.1 C rate under practically relevant conditions.

could be designed to further improve the solid-solid conversion kinetics in the future.

3. Conclusions

Guided by both experimental and computational studies, we identified MeTHF as a promising solvating molecule to stabilize RT Na–S batteries. With a proper solvation power and suitable molecular configuration, MeTHF could form a localized saturated electrolyte at a low salt-to-solvent ratio and diluent-to-solvent ratio, which has never been reported before. The solvent is found to not only tune ion-ion and ion-dipole interaction in the inner shell, but also regulate the anion-diluent interaction between the inner sheath and outer sheath. Theoretical simulation, 2D NMR, TOF-SIMS analyses suggest that a close Na^+-anion pair and relatively far Na^+-solvent distance in the inner sheath, coupled with a weak anion-diluent interaction is efficient for a stabilized Na-metal anode interface. Meanwhile, the saturated state of the LSE further pushes the limit of LHCE to transform the conventional sulfur conversion behavior, which enables a long-term Na–S cycling under practical conditions. This new solvation strategy may open new opportunities for liquid–liquid conversion batteries beyond Na–S.

Supporting Information

Supporting Information is available from the Wiley Online Library or from the author.

Acknowledgements

This work was supported by the U.S. Department of Energy, Office of Basic Energy Sciences, Division of Materials Science and Engineering under award number DE-SC0005397. Calculations at UT Austin were support by National Science Foundation (CHE-2102317) and the Texas Advanced Computing Center, and the National Energy Scientific Research Center.

Conflict of Interest

The authors declare no conflict of interest.

Data Availability Statement

The data that support the findings of this study are available from the corresponding author upon reasonable request.

Keywords

electrolyte regulation, sodium sulfur batteries, sodium-metal anode, solid-electrolyte interface, solvation structure

Received: January 27, 2023
Revised: March 9, 2023
Published online: April 27, 2023

[1] A. Manthiram, Y. Fu, S. H. Chung, C. Zu, Y. S. Su, *Chem. Rev.* **2014**, *114*, 11751.
[2] W. Guo, W. Zhang, Y. Si, D. Wang, Y. Fu, A. Manthiram, *Nat. Commun.* **2021**, *12*, 3031.
[3] J. Song, Y. Si, W. Guo, D. Wang, Y. Fu, *Angew. Chem., Int. Ed.* **2021**, *133*, 9969.
[4] D. Guo, X. Li, F. Ming, Z. Zhou, H. Liu, M. N. Hedhili, V. Tung, H. N. Alshareef, Y. Li, Z. Lai, *Nano Energy* **2020**, *73*, 104769.

[5] D. Guo, X. Li, W. Wahyudi, C. Li, A.-H. Emwas, M. N. Hedhili, Y. Li, Z. Lai, *ACS Nano* **2020**, *14*, 17163.
[6] A. Y. S. Eng, V. Kumar, Y. Zhang, J. Luo, W. Wang, Y. Sun, W. Li, Z. W. Seh, *Adv. Energy Mater.* **2021**, *11*, 2003493.
[7] Z. Yan, L. Zhao, Y. Wang, Z. Zhu, S. L. Chou, *Adv. Funct. Mater.* **2022**, *32*, 2205622.
[8] J. He, A. Bhargav, W. Shin, A. Manthiram, *J. Am. Chem. Soc.* **2021**, *143*, 20241.
[9] Y. Wang, D. Zhou, V. Palomares, D. Shanmukaraj, B. Sun, X. Tang, C. Wang, M. Armand, T. Rojo, G. Wang, *Energy Environ. Sci* **2020**, *13*, 3848.
[10] V. Kumar, A. Y. S. Eng, Y. Wang, D.-T. Nguyen, M.-F. Ng, Z. W. Seh, *Energy Storage Mater.* **2020**, *29*, 1.
[11] D. Guo, F. Ming, H. Su, Y. Wu, W. Wahyudi, M. Li, M. N. Hedhili, G. Sheng, L.-J. Li, H. N. Alshareef, Y. Li, Z. Lai, *Nano Energy* **2019**, *61*, 478.
[12] D. Guo, M. Li, M. N. Hedhili, V. Tung, Y. Li, Z. Lai, *Energy Storage Mater.* **2019**, *25*, 33.
[13] S. Tang, Q. Chen, Y. Si, W. Guo, B. Mao, Y. Fu, *Adv. Mater.* **2021**, *33*, 2100824.
[14] D. Guo, F. Ming, D. B. Shinde, L. Cao, G. Huang, C. Li, Z. Li, Y. Yuan, M. N. Hedhili, H. N. Alshareef, Z. Lai, *Adv. Funct. Mater.* **2021**, *31*, 2101194.
[15] X. Zheng, Z. Cao, Z. Gu, L. Huang, Z. Sun, T. Zhao, S. Yu, X.-L. Wu, W. Luo, Y. Huang, *ACS Energy Lett.* **2022**, *7*, 2032.
[16] X. Zheng, Z. Gu, X. Liu, Z. Wang, J. Wen, X. Wu, W. Luo, Y. Huang, *Energy Environ. Sci* **2020**, *13*, 1788.
[17] X. Xia, C. F. Du, S. Zhong, Y. Jiang, H. Yu, W. Sun, H. Pan, X. Rui, Y. Yu, *Adv. Funct. Mater.* **2021**, *32*, 2110280.
[18] G. G. Eshetu, G. A. Elia, M. Armand, M. Forsyth, S. Komaba, T. Rojo, S. Passerini, *Adv. Energy Mater.* **2020**, *10*, 2000093.
[19] Z. Tian, Y. Zou, G. Liu, Y. Wang, J. Yin, J. Ming, H. N. Alshareef, *Adv. Sci.* **2022**, *9*, 2201207.
[20] X. Cao, H. Jia, W. Xu, J.-G. Zhang, *J. Electrochem. Soc.* **2021**, *168*, 010522.
[21] L. Su, X. Zhao, M. Yi, H. Charalambous, H. Celio, Y. Liu, A. Manthiram, *Adv. Energy Mater.* **2022**, *12*, 2201911.
[22] Z. Yu, H. Wang, X. Kong, W. Huang, Y. Tsao, D. G. Mackanic, K. Wang, X. Wang, W. Huang, S. Choudhury, Y. Zheng, C. V. Amanchukwu, S. T. Hung, Y. Ma, E. G. Lomeli, J. Qin, Y. Cui, Z. Bao, *Nat. Energy* **2020**, *5*, 526.
[23] J. Holoubek, H. Liu, Z. Wu, Y. Yin, X. Xing, G. Cai, S. Yu, H. Zhou, T. A. Pascal, Z. Chen, P. Liu, *Nat. Energy* **2021**, *6*, 303.
[24] S. P. Beltran, X. Cao, J.-G. Zhang, P. B. Balbuena, *Chem. Mater.* **2020**, *32*, 5973.
[25] B. Nan, L. Chen, N. D. Rodrigo, O. Borodin, N. Piao, J. Xia, T. Pollard, S. Hou, J. Zhang, X. Ji, J. Xu, X. Zhang, L. Ma, X. He, S. Liu, H. Wan, E. Hu, W. Zhang, K. Xu, X. Q. Yang, B. Lucht, C. Wang, *Angew. Chem., Int. Ed.* **2022**, *61*, 202205967.
[26] L. P. Hou, Z. Li, N. Yao, C. X. Bi, B. Q. Li, X. Chen, X. Q. Zhang, Q. Zhang, *Adv. Mater.* **2022**, *34*, 2205284.
[27] Z. Cui, F. Zou, H. Celio, A. Manthiram, *Adv. Funct. Mater.* **2022**, *32*, 2203779.
[28] Z. Cui, Z. Guo, A. Manthiram, *Adv. Energy Mater.* **2023**, *13*, 2203853.
[29] Y. Chen, Z. Yu, P. Rudnicki, H. Gong, Z. Huang, S. C. Kim, J. C. Lai, X. Kong, J. Qin, Y. Cui, Z. Bao, *J. Am. Chem. Soc.* **2021**, *143*, 18703.
[30] X. Peng, T. Wang, B. Liu, Y. Li, T. Zhao, *Energy Environ. Sci* **2022**, *15*, 5350.
[31] R. Xu, X. Shen, X. X. Ma, C. Yan, X. Q. Zhang, X. Chen, J. F. Ding, J. Q. Huang, *Angew. Chem., Int. Ed.* **2021**, *60*, 4215.
[32] Z. Wu, R. Li, S. Zhang, L. lv, T. Deng, H. Zhang, R. Zhang, J. Liu, S. Ding, L. Fan, L. Chen, X. Fan, *Chem* **2023**, *9*, 650.
[33] B. D. Adams, J. Zheng, X. Ren, W. Xu, J. G. Zhang, *Adv. Energy Mater.* **2017**, *8*, 1702097.
[34] C. Wang, A. C. Thenuwara, J. Luo, P. P. Shetty, M. T. McDowell, H. Zhu, S. Posada-Perez, H. Xiong, G. Hautier, W. Li, *Nat. Commun.* **2022**, *13*, 4934.
[35] Y. Jin, P. M. L. Le, P. Gao, Y. Xu, B. Xiao, M. H. Engelhard, X. Cao, T. D. Vo, J. Hu, L. Zhong, B. E. Matthews, R. Yi, C. Wang, X. Li, J. Liu, J.-G. Zhang, *Nat. Energy* **2022**, *7*, 718.
[36] Z. W. Seh, J. Sun, Y. Sun, Y. Cui, *ACS Cent. Sci.* **2015**, *1*, 449.
[37] X. Zhou, Q. Zhang, Z. Zhu, Y. Cai, H. Li, F. Li, *Angew. Chem., Int. Ed.* **2022**, *61*, 202205045.
[38] J. Wu, Y. Tian, Y. Gao, Z. Gao, Y. Meng, Y. Wang, X. Wang, D. Zhou, F. Kang, B. Li, G. Wang, *Angew. Chem., Int. Ed.* **2022**, *61*, 202205416.